Acta Geochim (2024) 43:774–784
https://doi.org/10.1007/s11631-024-00699-x

ORIGINAL ARTICLE

Formation and growth of nanophase iron particles on the surface of Mercury revealed by experimental study

Ronghua Pang[1,2] · Yang Li[1,3] · Chen Li[1] · Pengfei Zhang[1] · Zhuang Guo[1,4] · Sizhe Zhao[1,5] · Han Yu[6] · Li Wang[6] · Chenxi Zhu[7] · Shuangyu Wang[8] · Kairui Tai[9] · Qinwei Zhang[10] · Yuanyun Wen[1] · Rui Li[1]

Received: 20 November 2023 / Revised: 12 April 2024 / Accepted: 24 April 2024 / Published online: 21 May 2024

Abstract Space weathering is a primary factor in altering the composition and spectral characteristics of surface materials on airless planets. However, current research on space weathering focuses mainly on the Moon and certain types of asteroids. In particular, the impacts of meteoroids and micrometeoroids, radiation from solar wind/solar flares/cosmic rays, and thermal fatigue due to temperature variations are being studied. Space weathering produces various transformation products such as melted glass, amorphous layers, iron particles, vesicles, and solar wind water. These in turn lead to soil maturation, changes in visible and near-infrared reflectance spectra (weakening of characteristic absorption peaks, decreased reflectance, increased near-infrared slope), and alterations in magnetism (related to small iron particles), collectively termed the "lunar model" of space weathering transformation. Compared to the Moon and asteroids, Mercury has unique spatial environmental characteristics, including more intense meteoroid impacts and solar thermal radiation, as well as a weaker particle radiation environment due to the global distribution of its magnetic field. Therefore, the lunar model of space weathering may not apply to Mercury. Previous studies have extensively explored the effects of micrometeoroid impacts. Hence, this work focuses on the effects of solar-wind particle radiation in global magnetic-field distribution and on the weathering transformation of surface materials on Mercury under prolonged intense solar irradiation. Through the utilization of high-valence state, heavy ion implantation, and vacuum heating simulation experiments, this paper primarily investigates the weathering transformation characteristics of the major mineral components such as anorthite, pyroxene, and olivine on Mercury's surface and compares them to the weathering transformation model of the Moon. The experimental results indicate that ion implantation at room temperature is insufficient to generate np-Fe^0 directly but can facilitate its formation, while prolonged exposure to solar thermal radiation on Mercury's surface can lead directly to the formation of np-Fe^0. Therefore, intense solar thermal radiation is a crucial component of the unique space weathering transformation process on Mercury's surface.

✉ Yang Li
liyang@mail.gyig.ac.cn

[1] Center for Lunar and Planetary Sciences, Institute of Geochemistry, Chinese Academy of Sciences, Guiyang, China

[2] University of Chinese Academy of Sciences, Beijing, China

[3] Center for Excellence in Comparative Planetology, Chinese Academy of Sciences, Hefei, China

[4] Institute of Remote Sensing and Geographical Information System, School of Earth and Space Sciences, Peking University, Beijing, China

[5] State Key Laboratory of Lunar and Planetary Sciences, Macau University of Science and Technology, Macau, China

[6] Faculty of Metallurgical and Energy Engineering, Kunming University of Science and Technology, Kunming, China

[7] State Key Laboratory of High Performance Ceramics and Superfine Microstructures, Shanghai Institute of Ceramics, Chinese Academy of Sciences, Shanghai, China

[8] Laboratory for Space Environment and Physical Sciences, Harbin Institute of Technology, Harbin, China

[9] Research Center for Planetary Science, College of Earth Science, Chengdu University of Technology, Chengdu, China

[10] Key Laboratory of Planetary Sciences, Purple Mountain Observatory, Chinese Academy of Sciences, Nanjing, China

Keywords Mercury · Space weathering · Np-Fe^0 · Solar thermal radiation · Solar wind

1 Introduction

Space weathering is the interaction between the space environment and the surface materials of airless bodies (Pieters et al. 2016; Grier and Rivkin 2018). Some planets in the solar system lack dense atmospheric protection, and global magnetic field shielding and are subject to temperature cycles due to periodic rotation. Processes such as (micro) meteoroid impacts, solar wind, solar flare particles, cosmic rays, and thermal fatigue due to diurnal temperature variations directly affect the surfaces of airless bodies (Pieters et al. 2016; Grier and Rivkin 2018). (Micro)meteoroid impacts can lead to fragmentation, melting, agglutination, vaporization, and deposition of surface materials. Solar wind, solar flare particles, and cosmic ray radiation, on the other hand, can induce particle implantation, sputtering, radiation damage, and amorphization on mineral surfaces, while thermal cycles lead to the disintegration and fragmentation of rocks and minerals (Pieters et al. 2016; Grier and Rivkin 2018). These space-weathering processes generate impact glasses, melt agglutinates, amorphous rims, iron particles, solar wind water, vesicle structures, and radiation tracks on planetary surfaces (Pieters et al. 2016; Grier and Rivkin 2018). These products then cause soil maturation, surface magnetic anomalies, increased spectral maturity of planetary regolith, and alteration of local redox environments (Pieters et al. 2016; Grier and Rivkin 2018; Guo et al. 2022). Therefore, the study of space weathering processes is crucial for the interpretation of spectral data, the assessment of regolith maturity, the understanding of regolith formation and spatiotemporal evolution, the study of lunar magnetic anomalies and their origin, and detection of local redox environment evolution on the lunar surface (Guo et al. 2022).

Compared to the Moon and asteroids, Mercury has unique characteristics in its space environment, including more intense meteoroid impacts and solar thermal radiation, as well as a weaker particle radiation environment due to the global distribution of its magnetic field (Sasaki and Kurahashi 2004; Christensen 2006; Domingue et al. 2014; Pieters et al. 2016; Kallio et al. 2019; Butkus et al. 2023; Zomerdijk-Russell et al. 2023; Zhong et al. 2024). However, the lunar model of space weathering transformation is not fully applicable to Mercury. This distinct space weathering environment on Mercury is a typical example of the formation and spatiotemporal evolution of regolith on airless planets in the solar system. Currently, exploration of Mercury primarily relies on remote sensing and ground-based observations, particularly spectral remote sensing. The space weathering of Mercury's regolith has a significant impact on its spectral remote sensing, particularly due to the formation of iron particles as a result of space weathering (Sasaki and Kurahashi 2004; Noble and Pieters 2007). Previous studies have shown that iron particles, including nanophase (np-Fe^0 and submicron (sm-Fe^0), are the primary cause of weakened characteristic absorption features. A large particle size (>40 nm) results in lower spectral reflectance (darkening), whereas a small particle size (<10 nm) increases the near-infrared slope of the spectra (reddening, Keller and Mckay 1993; Hapke et al. 2001; Noble and Pieters 2007). Since there are no samples returned from Mercury or meteorites, ground-based simulated experiments are the primary technical approach for studying the weathering transformation characteristics of Mercury's regolith.

The spectral data from the Messenger spacecraft indicates that Mercury has a lower spectral reflectance with less distinct absorption features than the Moon (Pieters et al. 2016; Trang et al. 2017; Trang and Lucey 2019). Moreover, spectral interpretation results reveal a higher content of sm-Fe^0 on Mercury's surface than on the Moon, particularly in high-magnesium regions (HMR) (Trang et al. 2017). Previous studies have suggested that iron particles on Mercury's surface are primarily formed during meteoroid impacts (Cirlin 1985; Anand et al. 2004; Guo et al. 2022; Li et al. 2022). It has been proposed that high temperatures may contribute to the growth of iron particles, but the understanding of the high-temperature processes induced by solar wind and solar thermal radiation on Mercury's surface remains incomplete (Noble and Pieters 2001; Trang et al. 2017). Additionally, other possible origins of iron particles have not been thoroughly investigated.

Regarding the mechanisms of space weathering, simulated experiments have been conducted, including laser radiation (Sasaki et al. 2001; Fazio et al. 2018; Weber et al. 2020), ion implantation (Dukes et al. 1999; Jäger et al. 2003; Kuhlman et al. 2015; Chrbolková et al. 2022), and high-temperature thermal cycling (Grier and Rivkin 2018; Yin et al. 2019). Previous research has predominantly focused on the interactions of main solar wind components (H^+, He^+, Ar^+, etc.) with material surfaces (Dukes et al. 1999; Jäger et al. 2003; Kuhlman et al. 2015; Chrbolková et al. 2022). Although H^+ and He^+ ion implantation experiments have produced Fe^0, there is no explicit high-resolution transmission electron microscopy (HRTEM) data to confirm the presence of np-Fe^0 (Dukes et al. 1999; Kuhlman et al. 2015; Cymes et al. 2023). Little is known about the reactions of high-valence, heavy ions from the solar wind with material surfaces. Iron ions in the solar wind primarily exist in the $+8$ to $+16$ valence states (Gruesbeck et al. 2013). Despite their low flux (Fe/H ~ 10^{-5}), these ions possess high energies (Schmid et al. 1987). It has not yet been investigated whether the implantation of iron ions in the high-valence state directly forms iron particles on mineral surfaces.

Additionally, experiments simulating high-temperature thermal cycles have focused only on their physical fragmentation, with no studies on their chemical processes (Grier and Rivkin 2018; Yin et al. 2019). There is also no study on whether iron particles can be directly formed at high temperatures on Mercury's surface.

This paper focuses on the unique characteristics of Mercury's space environment and chooses the formation of iron particles as the research focus under the global distribution of the magnetic field and the long-term intense solar irradiation (Biber et al. 2020; Bauch et al. 2021). By employing high-valence state Fe ion implantation and vacuum heating simulation experiments, the study primarily investigates the weathering transformation characteristics of major mineral components such as plagioclase, pyroxene, and olivine on Mercury's surface, as well as the mechanism of iron particle formation. The aim is to investigate whether iron particles could be directly formed on the surface of Mercury through the implantation of iron ions and high temperatures.

2 Samples and methods

Due to the absence of Mercury samples, Messenger's X-ray observations suggest that Mercury's surface is dominated by anorthite, magnesium olivine, pyroxene, and plagioclase (Namur and Charlier 2017). All samples used in these experiments are from Earth, including anorthite, magnesium olivine, pyroxene, and plagioclase. The anorthite is from the Vesuvian volcanic in Italy, An = 95. The olivine comes from the basalt inclusions in Damaping, Hebei Province, China, Fo = 91. The pyroxene is sourced from the Shigatse in Xizang Autonomous Region, China, primarily consisting of orthopyroxene. The plagioclase samples were purchased online, and their origin is unknown, but they mainly consist of potassium and sodium feldspar.

The ion implantation experiments were conducted using the 320 kV high-charge-state ion research platform at the Institute of Modern Physics, CAS, to implant Fe^{9+} ions into the samples. During the experiments, the equipment operated at a vacuum of approximately 1×10^{-3} Pa, an operating voltage of 50 kV, and an energy of 450 keV, reaching the energy range associated with high-speed solar wind velocities (Mckenzie 1998). The implantation dose was 2×10^{16} ions/cm^2, which is about 60 Ma implanted on the surface of Mercury (Sasaki and Kurahashi 2004; Kallio et al. 2019; Zhong et al. 2024).

The post-implantation samples were heated in a vacuum heating furnace independently constructed by Kunming University of Science and Technology. The schematic diagram of the vacuum heating furnace is shown in Fig. 1. During heating, the vacuum in the sample chamber was maintained at 8.6×10^{-3} Pa. The heating temperature was set to 400 ℃, which corresponds approximately to the extremes at equatorial and low-latitude regions (Bauch et al. 2021). The samples were held at this temperature for 4 and 8 h. The temperature was then increased to 500 °C for 4 h to facilitate the accelerated production of np-Fe^0.

Sample selection and transmission electron microscope (TEM) sample preparation were performed utilizing the FEIScios dual beam scanning electron microscope (SEM/FIB) at the Institute of Geochemistry, CAS. This equipment includes a field emission scanning electron microscope, a gallium ion gun, secondary electron detectors, backscattered electron detectors, and an EDAX ELECT SUPER 70 mm^2 energy dispersive X-ray spectroscopy (EDS) system. Ga ion beam was used to cut and thin the samples, ultimately achieving a sample thickness of approximately 100 nm.

The composition and structure of the sample were analyzed using the FEI Talos F200X transmission electron microscope (TEM) at the Suzhou Institute of Nano-Tech and Nano-Bionics, CAS, with an operating voltage of 200 kV.

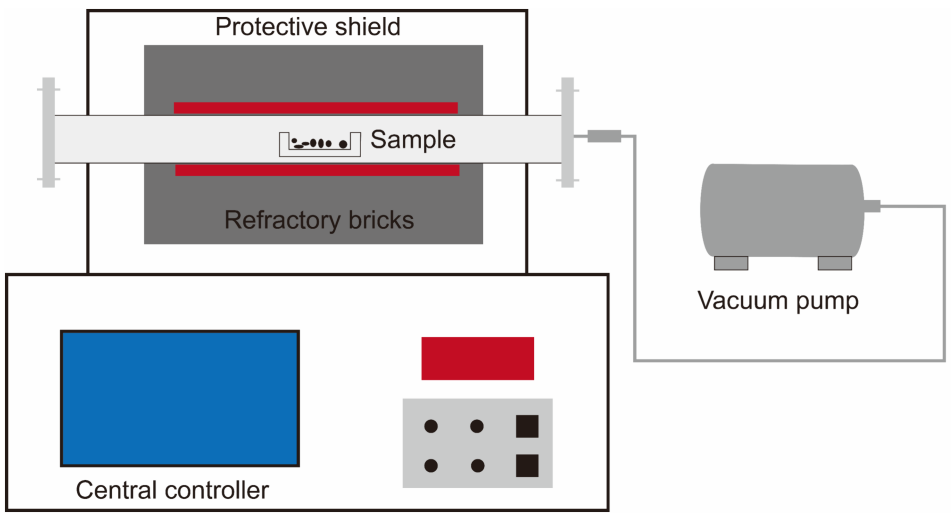

Fig. 1 The schematic diagram of the vacuum heating furnace

HRTEM, high angle annular dark field, selected area electron diffraction, and energy dispersive spectrometer mapping (EDS mapping) data of the sample were obtained.

3 Results

3.1 Ion implantation results

Implantation of Fe^{9+}, Figs. 2a, b, c, and e present TEM images of FIB sections of pyroxene, potassium feldspar, olivine, and anorthite, respectively. These images reveal the formation of a uniform amorphous layer on the minerals' surfaces, which is 500–600 nm thick (Fig. 2a–c, d). The thickness slightly varied depending on the type of mineral. The amorphous layer maintained a high degree of uniformity and contained no dark material particles or vesicles (Fig. 1a–c, d).

Results from EDS surface scanning and line scanning confirmed that the implanted iron ions were primarily concentrated in the central region of the amorphous layer (Fig. 2d, f, g). This distribution adhered to the characteristics of a normal distribution and corresponded to previous theoretical calculations (Li et al. 2014). Furthermore, dislocations were observed in the mineral crystals due to ion implantation, mainly occurring near the bottom of the amorphous layer (Fig. 2a, b, c, e).

3.2 Vacuum heating

Heating was carried out at 400 °C for 4 h in a vacuum furnace. Unfortunately, the sample preparation was not successful due to the displacement of plagioclase during the FIB sectioning process. For the anorthite and pyroxene, it was observed that the thickness of the amorphous layer remained unchanged, and the heat treatment did not eliminate dislocations (Fig. 3a, e, g).

Analysis through TEM-EDS mapping revealed that that the implanted iron was still concentrated in the central area of the amorphous layer even after a 4 h heat treatment of the samples at 400 °C (Fig. 3c, d, f, j, k). Notably, pyroxene naturally contains iron, leading to a higher iron concentration within the amorphous layer compared to anorthite. Thus, some dark, non-crystallized particles were

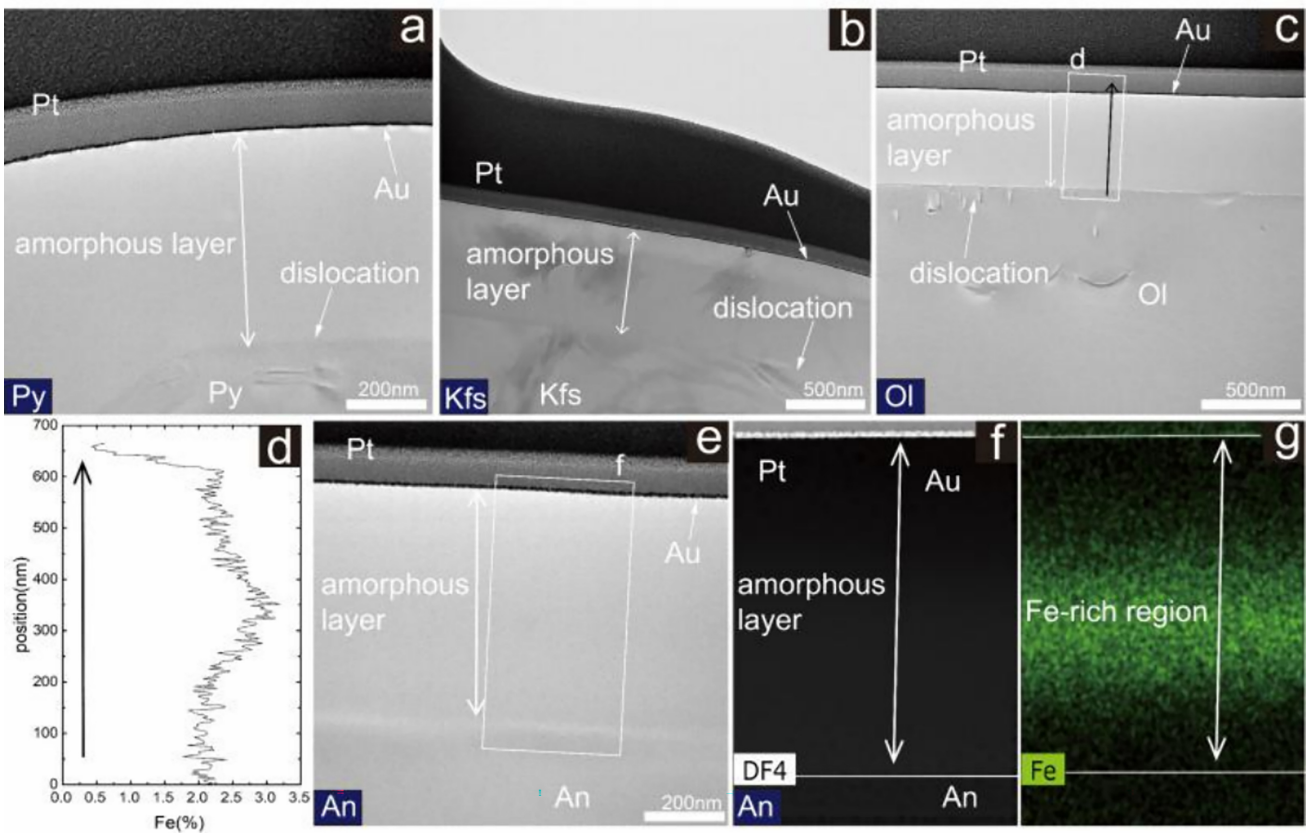

Fig. 2 The TEM results after ion implantation **a** TEM image of the pyroxene; **b** TEM image of the potassium feldspar; **c** TEM image of the olivine have amorphous layer; **d** TEM-EDS line scan of the olivine amorphous layer, iron elements enrichment in amorphous layer; **e** TEM image of the anorthite; **f** and **g** TEM-EDS mapping of iron elements in the amorphous layer of anorthite, iron elements enrichment in amorphous layer

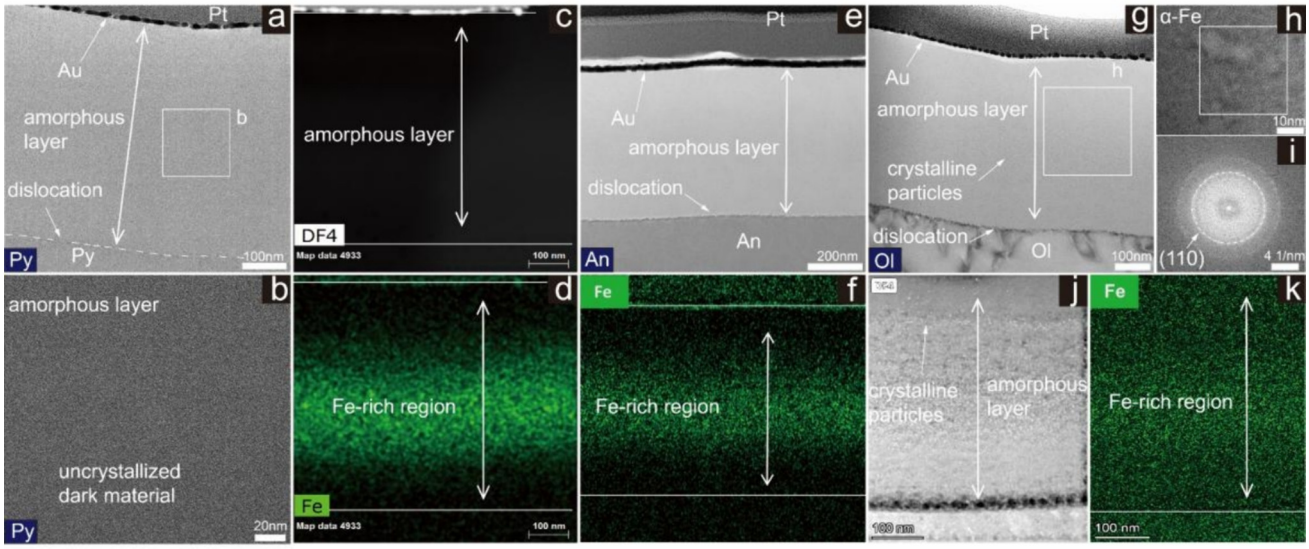

Fig. 3 The results after a 4 h heat treatment at 400 °C: **a** TEM image of the pyroxene; **b** Pyroxene's amorphous layer displaying uncrystallized dark material; **c** and **d** TEM-EDS mapping of iron elements within the amorphous layer of pyroxene, illustrating iron enrichment in the central part of the amorphous layer; **e** TEM image of the anorthite; **f** TEM-EDS mapping of iron elements within the amorphous layer of anorthite, demonstrating iron enrichment in the middle of the amorphous layer; **g** TEM image of the olivine; **h** HRTEM image revealing crystallized dark material within the amorphous layer of olivine; **i** FFT representation for the [110] zone axis of α-Fe, with the FFT area indicated by the panel region in (**h**); **j** and **k** TEM-EDS mapping of iron elements within the amorphous layer of olivine, with iron enrichment in the central region of the amorphous layer

observed in the amorphous layer of pyroxene (Fig. 3a-f), while this phenomenon was less evident in the amorphous layer of anorthite (Fig. 3e).

Within the amorphous layer of olivine, however, an abundance of dark crystalline particles with diameters of 1–3 nm was discovered, which were mainly concentrated in the upper and middle sections of the amorphous layer (Fig. 3g, h, j). After the fast Fourier transform (FFT) lattice calibration, these particles were identified as $\alpha-Fe$ with a [110] zone axis (Fig. 3g–k). It is important to note that no dark crystalline particles were observed in the olivine substrate itself (Fig. 3g).

After the first 4 h heating at 400 °C, a further 4 h heating at the same temperature was carried out. Notably, the amorphous layer's thickness in the sample remained unchanged and dislocations persisted at the interface between the substrate and the amorphous layer (Fig. 4a, c, e, h). No dark crystalline particles were detected in the anorthite and pyroxene samples. However, there was clear evidence of non-crystallized dark material (Fig. 4a–d). These non-crystallized dark materials were found to correlate with the distribution of iron.

Numerous dark crystalline particles with a diameter of 2–3 nm each were identified in both the amorphous layer and the olivine substrate. By combining HRTEM images with lattice calibration, these particles were found to be $\alpha-Fe$ (Fig. 4e–j). The α-Fe within both the amorphous layer and the substrate exhibited a [110] zone axis diffraction ring, and the olivine substrate displayed a [222] zone axis.

After the 8 h heating period at 400 °C, the temperature was increased to 500 °C for a further 4 h to expedite the generation of np-Fe^0. However, similar to the 8 h heating at 400 °C, no change in the thickness of the amorphous layer in the sample was observed, and dislocations were still visible at the interface between the substrate and the amorphous layer (Fig. 5a, b, c, e). No dark crystalline particles were detected in the anorthite and pyroxene samples, but conspicuous uncrystallized dark material, closely resembling the Fe distribution, was observed predominantly in the middle of the amorphous layer (Fig. 5a–d). Additionally, a few vesicles were identified in the pyroxene sample, possibly linked to the sample's composition (Fig. 5a–b).

Both the amorphous layer and the olivine substrate contained a significant quantity of dark crystalline particles. By combining HRTEM images and lattice calibration, these were verified as α-Fe particles (Fig. 5e–h). Notably, olivine crystals coexisted with α-Fe particles within the substrate (Fig. 5g–h). The FFT analysis confirmed that these particles have the [110] zone axis of α-Fe and the [101], [002], and [-101] zone axes of olivine. Compared to the conditions of 8 h heating at 400 °C, the 4 h heating at 500 °C significantly increased the amount of np-Fe^0 (Figs. 4g, i, 5f, g).

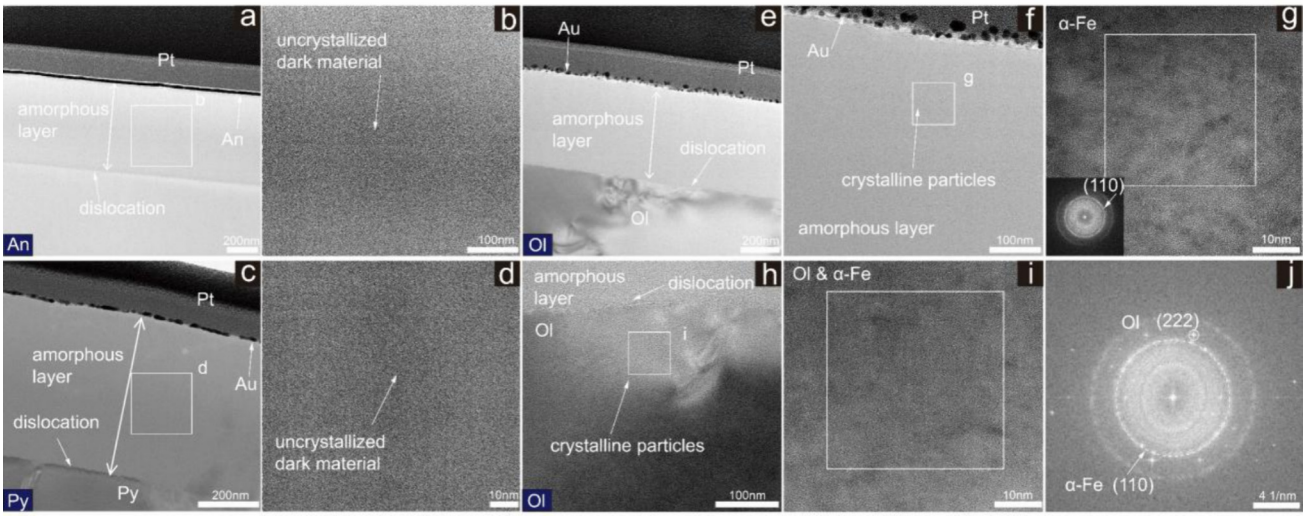

Fig. 4 The results after 8 h heating at 400 °C. **a** TEM image of the anorthite; **b** Anorthite`s amorphous layer displaying uncrystallized dark material; **c** TEM image of the pyroxene; **d** Pyroxene amorphous layer showing uncrystallized dark material; **e** and **f** TEM image of olivine; **g** HRTEM image revealing crystallized particles within olivine's amorphous layer, with the FFT for the [110] zone axis of α-Fe inserted in the bottom-left corner; **h** TEM image of olivine substrate; **i** HRTEM image of olivine substrate and α-Fe particles; **j** The FFT for the [110] zone axis of α-Fe and [222] zone axis of olivine

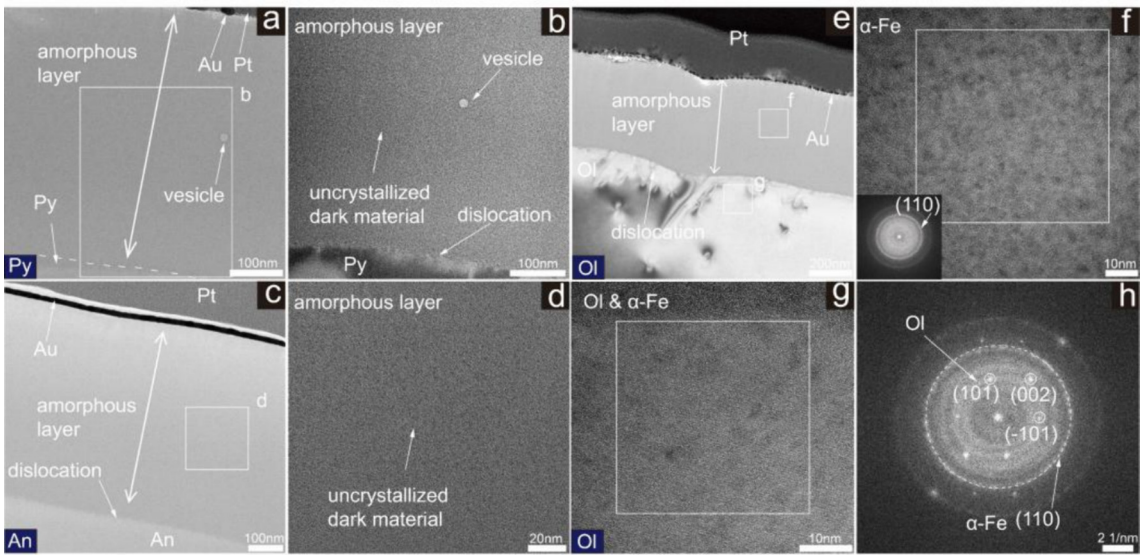

Fig. 5 The results after heating at 400 °C for 8 h and subsequent heating at 500 °C for 4 h: **a** TEM image of the pyroxene; **b** uncrystallized dark material within the pyroxene`s amorphous layer; **c** TEM image of the anorthite; **d** anorthite amorphous layer displaying uncrystallized dark material; **e** TEM image of the olivine; **f** HRTEM image revealing crystallized particles within olivine's amorphous layer, with the FFT for the [110] zone axis of α − Fe inserted in the lower-left corner; **g** HRTEM image displaying both olivine substrate and crystallized dark particles; **h** The FFT for the [110] zone axis of α-Fe and the [101], [002], and [− 101] zone axes of olivine

4 Discussion

4.1 The effect of ion implantation

Previous studies proposed mechanisms for the reduction of Fe^{2+} to np-Fe^0 by H^+ interactions in the solar wind (Housley et al. 1972, 1974; Morris 1977, 1980; Taylor and Cirlin, 1985). However, simulation experiments have not provided reliable evidence for the formation of np-Fe^0 (Dukes et al. 1999; Jäger et al. 2003; Kuhlman et al. 2015; Chrbolková et al. 2022; Cymes et al. 2023). Our experimental findings align with prior research, following Fe^{9+} implantation, we

observed the exclusive formation of a highly uniform amorphous layer on the mineral surface containing no np-Fe^0 (Fig. 2a–c, e). The implanted Fe aggregated in the middle of the amorphous layer, and the depth of our induced amorphous layer surpassed that generated by Chrbolková (2022; Fig. 1) due to the high ionic energy (Fig. 2c, d, f, g). Notably, our implanted ions differed from the work of Chrbolková et al. (2022), as we could not form a significant number of vesicles within the amorphous layer (Fig. 2a–c, e). The variance of the implanted ions is probably the reason for this difference. In other studies, H^+ and He^+ ions may generate He, H_2, and H_2O, causing vesicle formation in the amorphous layer. In our experiment, Fe^{9+} potentially combined with oxygen, forming oxides that do not produce vesicles and np-Fe^0. The implanted Fe^{9+} may not form np-Fe^0 directly due to its high valence state or low content, and the low temperature is also a factor that inhibits the formation of np-Fe^0. It is challenging to generate np-Fe^0 directly by ion implantation alone at room temperature.

In our experiments, the amorphous layer of olivine produced np-Fe^0 after heating at 400 °C for 4 h (Fig. 3g–i), whereas olivine crystals formed np-Fe^0 when heated at 400 °C for 8 h (Fig. 4h–j). The earlier formation of np-Fe^0 in the amorphous layer can be attributed to two primary factors:

(i) The formation of the amorphous layer makes it easier for Fe to aggregate and form np-Fe^0. During the ion implantation process, collisions cause the displacement of ions (O, Si, Fe, Mg) within the mineral crystals, leading to the disruption of the mineral crystal structure and the subsequent formation of an amorphous layer (Li 2013). This amorphous layer formation increases the likelihood of particle displacement, rendering Fe atoms more prone to crystallization (Li 2013).

(ii) The implantation of Fe ions results in an increased Fe content in the amorphous layer, facilitating the formation of np-Fe^0, as depicted in Fig. 2j. Following Fe^{9+} implantation with a dose of 2×10^{16} ions/cm^2, the Fe content in the mineral's amorphous layer increased by approximately 0.1 wt%, but no dark particles were observed (Fig. 2a, c, e). No np-Fe^0 was formed in anorthite, despite heating at 400 °C for 8 h and 500 °C for 4 h, only non-crystallized dark particles were observed (Fig. 3e, Fig. 4a, b, Fig. 5c, d). Conversely, np-Fe^0 formed in the amorphous layer of olivine after only 4 h of heating at 400 °C (Fig. 3g–i). This observation suggests that the implanted Fe content at this dose may not be sufficient to crystallize and form np-Fe^0. In the amorphous olivine layer, np-Fe^0 can provide Fe mainly by itself. Considering prolonged exposure to Mercury's surface, our implantation dose likely mirrors the 60 Ma Fe ion implantation dose there (Sasaki and Kurahashi 2004; Zhong et al. 2024). Extended exposure leads to higher Fe implantation doses and heating times, allowing np-Fe^0 to form on the feldspathic surface. In the case of Fe^{n+} ion implantation, a higher dose (or Fe content) is essential to produce np-Fe^0 at the same temperature.

4.2 The difference between olivine and pyroxene

During the entire heating process of pyroxene, np-Fe^0 did not occur at any point (Fig. 3a, b, Fig. 4c, d, Fig. 5a, b). In contrast, olivine crystals formed np-Fe^0 under heating at 400 °C for 8 h (Fig. 4h–j). This aligns with previous research findings that suggest a higher threshold for the formation of np-Fe^0 in pyroxene (Yamada et al. 1999; Li 2013). Specifically, under identical ion implantation and temperature heating conditions, the production of np-Fe^0 in pyroxene is more difficult than in olivine (Yamada et al. 1999; Li 2013; Chrbolková et al. 2022). According to Hiroi and Takeda (1991), the diffusion coefficient of Fe in olivine and pyroxene differs, with Fe diffusion occurring significantly faster in olivine than in pyroxene. However, in our experiments, the amorphous layer of pyroxene consistently failed to produce np-Fe^0. We consider iron content may also play an important role. Further investigation is needed to discern the specific reasons for np-Fe^0 production differences in pyroxene and olivine and to elucidate the effects of variations in their structure and composition.

4.3 Effect of heating on the formation and growth of iron particles in olivine on the surface of Mercury

After heating at 400 °C for 8 h, olivine crystals formed np-Fe^0 (Fig. 4h–j). Due to the specific characteristics of the samples, the TEM–EELS tests did not provide meaningful data for the np-Fe^0 generated after heating, so it was impossible to ascertain the mechanism behind the formation of np-Fe^0 through changes in the oxidation state of Fe. Currently, there are three main explanations for the origin of np-Fe^0 in space weathering: vapor deposition during meteorite impact (Anand et al. 2004), the disproportionation reaction (Guo et al. 2021; Li et al. 2022), and thermal decomposition of Fe-Mg silicates (Guo et al. 2020, 2022a). Since there is no meteorite impact simulation involved, the vapor deposition process is not implicated in our experiment. The thermal decomposition of Fe–Mg silicates results in the production of np-Fe^0 and vesicles (Guo et al. 2020, 2022a). In contrast, our TEM results reveal the absence of significant vesicles around np-Fe^0 (Fig. 3e–h, Fig. 4e–i, Fig. 5e–g). Combining our research findings with previous studies (Guo et al. 2020, 2021, 2022a; Li et al. 2022), the disproportionation reaction may be responsible for forming

np-Fe^0 in olivine. However, this is a speculative assumption. There might be other undiscovered formation mechanisms that will be investigated in future work.

Our vacuum heating experiments have revealed that a minute quantity of Fe within forsterite can swiftly nucleate, leading to the formation of np-Fe^0 when surface temperatures are like those on Mercury (Fig. 4e–j). Given Mercury's extended rotation period, characterized by prolonged periods of elevated surface temperatures, np-Fe^0 can continue to grow over longer heating periods. Therefore, considering the limitations of our experimental conditions, we have referred to previous knowledge (Noble and Pieters 2001; Trang et al. 2017) and integrated the growth principles of small particles from materials science theory to offer a potential explanation for the growth of np-Fe^0.

In materials science, the growth of small particles is predominantly governed by factors such as diffusion, convection, interfacial energy, Ostwald ripening, Brownian motion, and others (Li and Deepak 2022). Considering the internal conditions of magnesium olivine on the surface of Mercury, the growth of np-Fe^0 is primarily influenced by diffusion and the Ostwald ripening process (Noble and Pieters 2001; Li and Deepak 2022). After nucleation, np-Fe^0 grows due to a substantial oversaturation of the surrounding matrix. The concentration of Fe atoms in the matrix decreases in the vicinity of np-Fe^0, which results in highly concentrated Fe atoms diffusing to the particles from a distance. As np-Fe^0 continues to grow autonomously, these particles, compelled by concentration gradients, approach each other, undergo deformation, establish liquid bridges, and eventually coalesce into larger particles (Tanaka 1995, 1996).

If np-Fe^0 continues to grow and reaches a point where the Fe concentration in the matrix decreases to a certain level, the iron particle growth is then predominantly governed by the Ostwald ripening process. During this phase, the matrix around the large iron particles remains oversaturated, while it becomes undersaturated for the smaller iron particles. As a result, large iron particles continue to grow through diffusion, while small iron particles dissolve and vanish (Yao et al. 1993; Li and Deepak 2022). Noble and Pieters (2001) were the pioneers in investigating this process as a growth mechanism of iron particles on the surface of Mercury. Due to limitations in our experimental conditions, we adapted their formula to our experimental setup. The results indicate that under heating at 400 °C, np-Fe^0 in magnesium olivine reaches the particle size (~40 nm) that induces spectral darkening (Noble et al. 2007). Over several million years, the formation of sm-Fe^0 can be observed (Fig. 6).

$$r^3 - r_0^3 = \frac{8}{9} \times \frac{x_{IL}\left(1 - x_{IL}\right)}{(x_{IS} - x_{IL})^2} \times \frac{D\Omega\sigma}{RTI} \times \left(t - t_0\right)$$

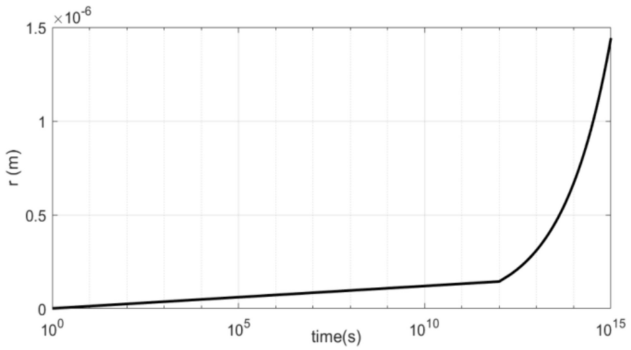

Fig. 6 Variation of np-Fe^0 particle size with time under 400 °C heating. Np-Fe^0 can be grown to sm-Fe^0 in a few Ma

r_0 = original size of Fe particles $\approx$ 1nm = 1×10^{-9}m

x_{IL} = fraction of np − Fe^{0}in olivine $\approx$ 0.1

x_{IS} = fraction of olivine = 1

D =diffusion coefficient of Fe in olivine $\approx 10^{-24}$ m^2/s(Chakraborty, 2010)

Ω = molar volume of Fe = 7.09×10^{-6}m^3/mol

σ = surface energy = 2400 mJ/m^2(Tyson, 1977)

R = thermodynamic constant = 8.314×10^3mJ/(mol × K)

T = experimental temperature = 673 K

I = thermodynamic factor $\approx$ 1

$t - t_0$ = heating time

In connection with earlier relevant research results and experiments, we assume that np-Fe0 is formed during the vapor deposition of meteorite impact on the Mercury surface and that np-Fe^0 and sm-Fe^0 are present in the molten glass generated by the impact (Cintala 1992, Fig. 7a). Implantation and sputtering on the surface of Mercury due to the prolonged exposure to solar wind may also contribute to the formation of np-Fe^0 (Fig. 7a). Additionally, under the continuous influence of solar thermal radiation, Fe–Mg silicate minerals have the potential to form np-Fe^0, with solar wind-implanted Fe potentially playing a role in promoting the formation of np-Fe^0 in the amorphous layer.

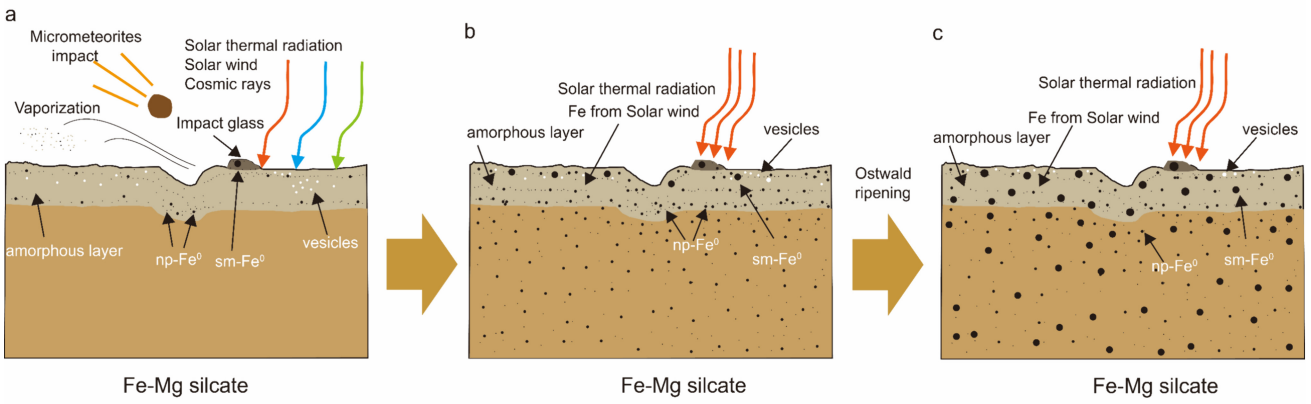

Fig. 7 Diagram of the formation of the np-Fe^0 and sm-Fe^0 on the surface of Mercury. **a** Meteorite impacts and solar wind (including Fe implanted by the solar wind) on the surface of Mercury form np-Fe^0 and sm-Fe^0, **b** Solar thermal radiation results in the formation and growth of np-Fe^0; **c** Solar thermal radiation leads to further growth of iron particles

These iron particles undergo Ostwald ripening, facilitating further growth and the eventual formation of sm-Fe^0 (Fig. 6, Fig. 7b, c).

Data from the Messenger X-ray spectrometer reveals the presence of the HMR on the surface of Mercury. The primary mineral in this region is magnesium olivine (Namur and Charlier 2017; Trang et al. 2017; Frank et al. 2017; Nittler et al. 2020). The spectrum of the HMR appears relatively dark, exhibiting a less pronounced reddening of the spectral slope (Izenberg et al. 2013). In our experiments, we found that magnesium olivine can rapidly form np-Fe^0 and sm-Fe^0, which seems to explain the spectral characteristics of HMR.

The rapid formation of np-Fe^0 and sm-Fe^0 on the surface of Mercury, caused by various factors, can significantly affect the spectral properties of the surface, especially in an environment containing reducing substances such as graphite. Therefore, when interpreting the spectrum of Mercury's surface, the influence of optically opaque particles of various origins must be fully taken into account. The dominant factors for the formation of np-Fe^0 and sm-Fe^0 in different regions must be analyzed separately.

5 Conclusions

By comparing the results of different temperatures and different minerals in the process of implantation and heating, combined with thermodynamic calculations, we draw the following conclusions:

1. Fe^{9+} ion implantation alone is a challenge to facilitate the formation of np-Fe^0 at normal temperature;
2. Ion implantation or an increased Fe content can significantly reduce the threshold for the formation of np-Fe^0;
3. Compared to magnesium olivine, pyroxene is less prone to generate np-Fe^0;
4. The surface temperature of Mercury can induce magnesium olivine to form np-Fe^0 within a relatively short period (a few hours) and sm-Fe^0 within a few million years, changing its spectral characteristics.

Acknowledgements Thanks to the 320kV highly charged ion comprehensive research platform provided by the Institute of Modern Physics, CAS for the experimental support, thanks to engineers Tongmin Zhang and Fuhe Wang of the Institute of Modern Physics, CAS for their help during the experiment. David T. Blewett of Johns Hopkins University also provides some literature support in the discussion. This work was supported by the Strategic Priority Research Program of the Chinese Academy of Sciences (XDB 41000000), the National Natural Science Foundation of China (42273042 and 41931077), the Youth Innovation Promotion Association, the Chinese Academy of Sciences (2020395), the Guizhou Provincial Science and Technology Projects (QKHJC-ZK [2023]-General 473).

Author contributions Ronghua Pang: Validation, Investigation, Experiment, Data Curation, Writing -Original Draft, Writing—Review & Editing; Yang Li: Conceptualization, Writing—Original Draft, Writing—Review & Editing, Supervision, Project administration, Funding acquisition; Chen Li: Writing—Original Draft, Writing—Review & Editing; Pengfei Zhang: Writing—Original Draft, Writing—Review & Editing; Zhuang Guo: Writing—Original Draft, Writing—Review & Editing; Sizhe Zhao: Writing—Original Draft, Writing—Review & Editing; Han Yu: Vacuum heating; Li Wang: Vacuum heating; Chenxi Zhu: Micro-Structure analysis; Shuangyu Wang: Visualization; Kairui Tai: Sample treatment, Micro-Structure analysis; Qinwei Zhang: Writing—Original Draft; Yuanyun Wen: Micro-Structure analysis; Rui Li: Micro-Structure analysis, Funding acquisition.

Declarations

Conflict of interest On behalf of all authors, the corresponding author states that there is no conflict of interest.

References

Anand M, Taylor LA, Nazarov MA, Shu J, Mao HK, Hemley RJ (2004) Space weathering on airless planetary bodies: clues from the lunar mineral hapkeite. Proc Natl Acad Sci USA 101(18):6847–6851

Bauch KE, Hiesinger H, Greenhagen BT, Helbert J (2021) Estimating surface temperatures on Mercury in preparation of the MERTIS experiment onboard BepiColombo. Icarus 354:114083

Biber H, Szabo PS, Jäggi N, Wallner M, Stadlmayr R, Moro MV, Aumayr F (2020) Solar wind Helium ion interaction with Mg and Fe rich pyroxene as Mercury surface analogue. Nucl Instrum Methods Phys Res Sect B 480:10–15

Butkus CR, Warren AO, Kite ES, Torres S, Naoz S, Glass JB (2023) A note on graphite hydrogenation as a source of abiotic methane on rocky planets: a case study for Mercury. Icarus 400:115580

Chrbolková K, Halodová P, Kohout T, Ďurech J, Mizohata K, Malý P, Jarugula R (2022) Sub-surface alteration and related change in reflectance spectra of space-weathered materials. Astron Astrophys 665:A14

Christensen UR (2006) A deep dynamo generating Mercury's magnetic field. Nature 444(7122):1056–1058

Cintala MJ (1992) Impact-induced thermal effects in the lunar and Mercurian regoliths. J Geophys Res Planets 97(E1):947–973

Cirlin EH, Taylor LA, and Lofgren GE (1985, March). Fe/Mg KD for olivine/liquid in chondrules: effects of cooling rate. In: LUNAR AND PLANETARY SCIENCE XVI, PP. 133–134. Abstract (Vol. 16, pp. 133–134)

Cymes BA, Burgess KD, Stroud RM (2023) Detection of ferric iron in an exsolved lunar pyroxene using electron energy loss spectroscopy (EELS): implications for space weathering and redox conditions on the Moon. Meteorit Planet Sci 58(2):259–274

Domingue DL, Chapman CR, Killen RM, Zurbuchen TH, Gilbert JA, Sarantos M, McClintock WE (2014) Mercury's weather-beaten surface: understanding Mercury in the context of lunar and asteroidal space weathering studies. Space Sci Rev 181:121–214

Dukes CA, Baragiola RA, McFadden LA (1999) Surface modification of olivine by H^+ and He^+ bombardment. J Geophys Res Planets 104(E1):1865–1872

Fazio A, Harries D, Schmidt D, Pollok K, Langenhorst F (2018) From laser experiments to nature: how accurately can we reproduce space weathering? Eur Planet Sci Congress 12:EPSC2018–EPSC2683

Frank EA, Potter RW, Abramov O, James PB, Klima RL, Mojzsis SJ, Nittler LR (2017) Evaluating an impact origin for Mercury's high-magnesium region. J Geophys Res Planets 122(3):614–632

Grier J, Rivkin AS (2018) Airless bodies of the inner solar system: Understanding the process affecting rocky, airless surfaces. Elsevier Amsterdam

Gruesbeck JR (2013) Exploring the origin of coronal mass ejection plasma from *in-situ* observations of ionic charge state composition (Doctoral dissertation)

Guo Z, Li Y, Liu S (2020) Discovery of nanophase iron particles and high pressure clinoenstatite in a heavily shocked ordinary chondrite: implications for the decomposition of pyroxene-sciencedirect. Geochim Cosmochim Acta 272:276–286

Guo Z, Li Y, Chen H (2021) Evidence for the disproportionation of iron in a eucrite meteorite: implications for impact processes on vesta. J Geophys Res Planets 126(8):1910–1924

Guo Z, Li C, Li Y, Wen Y, Wu Y, Jia B, Ouyang Z (2022) Sub-microscopic magnetite and metallic iron particles formed by eutectic reaction in Chang'E-5 lunar soil. Nat Commun 13(1):7177

Guo Z, Li C, Li Y, Wen Y, Tai K, Li X, Ouyang Z (2022a) Nanophase iron particles derived from fayalitic olivine decomposition in Chang'E-5 lunar soil: Implications for thermal effects during impacts. Geophys Res Lett 49(5):e2021GL097323

Hapke B (2001) Space weathering from Mercury to the asteroid belt. J Geophys Res Planets 106(E5):10039–10073

Hiroi T, Takeda H (1991) Reflectance spectroscopy and mineralogy of primitive achondrites-lodranites. In: Fifteenth symposium on antarctic meteori 4, p. 163

Housley RM, Grant RW, Abdel-Gawad M (1972) Study of excess Fe metal in the lunar fines by magnetic separation Mössbauer spectroscopy, and microscopic examination. In: Lunar and Planetary Science Conference Proceedings 3, p 1065

Housley RM, Cirlin EH, Paton NE, Goldberg IB (1974) Solar wind and micrometeorite alteration of the lunar regolith. In: Lunar science conference, 5th, Houston, Tex., March 18–22, 1974, Proceedings. Volume 3. (A75–39540 19–91) New York, Pergamon Press Inc 5, pp 2623–2642

Izenberg NR, Weider SZ, Nittler LR, Solomon SC (2013) Correlating reflectance and X-Ray spectroscopic data from MESSENGER. In: 44th annual lunar and planetary science conference 1719, p 3018

Jäger C, Fabian D, Schrempel F, Dorschner J, Henning T, Wesch W (2003) Structural processing of enstatite by ion bombardment. Astron Astrophys 401(1):57–65

Kallio E, Dyadechkin S, Wurz P, Khodachenko M (2019) Space weathering on the Moon: farside-nearside solar wind precipitation asymmetry. Planet Space Sci 166:9–22

Keller LP, McKay DS (1993) Discovery of vapor deposits in the lunar regolith. Science 261(5126):1305–1307

Keller LP, Mckay DS (1997) The nature and origin of rims on lunar soil grains. Geochim Et Cosmochimixa Acta 31(11):1034–1048

Kuhlman KR, Sridharan K, Kvit A (2015) Simulation of solar wind space weathering in orthopyroxene. Planet Space Sci 115:110–114

Li Y (2013) Microstructure characters of lunar main minerals induced in solar wind radiation and experimental study. University of Chinese Academy of Science Beijing

Li J, Deepak FL (2022) *In-situ* kinetic observations on crystal nucleation and growth. Chem Rev 122(23):16911–16982

Li Y, Li XY, Wang SJ, Li SJ, Tang H (2014) SRIM stimulation of Proton`s role in the radiation of lunar enstatite. Bull Mineral Petrol Geochem 33:71–76

Li C, Guo Z, Li Y, Tai K, Wei K, Li X, Ma W (2022a) Impact-driven disproportionation origin of nanophase iron particles in Chang'E-5 lunar soil sample. Nat Astronomy 6(10):1156–1162

McKenzie JF, Sukhorukova GV, Axford WI (1998) The source region of the fast solar wind. Astro Astrophys 330:1145–1148

Morris RV (1977) Origin and evolution of the grain-size dependence of the concentration of fine-grained metal in lunar soils-The maturation of lunar soils to a steady-state stage. In: Lunar Science Conference, 8th, Houston, Tex., March 14–18, 1977, Proceedings. Volume 3. (A78–41551 18–91) New York Pergamon Press Inc Vol. 8, pp 3719–3747

Morris, RV (1980) Origins and size distribution of metallic iron particles in the lunar regolith. In: Lunar and Planetary Science Conference, 11th, Houston, TX, March 17–21, 1980, Proceedings. Volume 2. (A82-22296 09-91) New York Pergamon Press (Vol. 11, pp. 1697–1712)

Namur O, Charlier B (2017) Silicate mineralogy at the surface of Mercury. Nat Geosci 10(1):9–13

Nittler LR, Frank EA, Weider SZ, Crapster-Pregont E, Vorburger A, Starr RD, Solomon SC (2020) Global major-element maps of Mercury from four years of MESSENGER X-Ray Spectrometer observations. Icarus 345:113716

Noble SK, Keller LP, Pieters CM (2007) An experimental approach to understanding the optical effects of space weathering. Icarus 192(2):629–642

Noble SK, Pieters CM (2001) Space weathering in the Mercurian environment. Mercury: Space Environment, and Surface and Interior

Pieters CM, Noble SK (2016) Space weathering on airless bodies. J Geophys Res Planets 121(10):1865–1884

Sasaki S, Kurahashi E (2004) Space weathering on Mercury. Adv Space Res 33(12):2152–2155
Sasaki S, Nakamura K, Hamabe Y, Kurahashi E, Hiroi T (2001) Production of iron nanoparticles by laser irradiation in a simulation of lunar-like space weathering. Nature 410(6828):555–557
Schmid J, Bochsler P, Geiss J (1987) Velocity of iron ions in the solar wind. J Geophys Res Space Physics 92(A9):9901–9906
Tanaka H (1995) A new coarsening mechanism of droplet spinodal decomposition. J Chem Phys 103(6):2361–2364
Tanaka H (1996) Coarsening mechanisms of droplet spinodal decomposition in binary fluid mixtures. J Chem Phys 105(22):10099–10114
Taylor SR (1982) Planetary science: a lunar perspective. Lunar and Planetary Institute Houston
Taylor LA, Cirlin EH (1985) A review of ESR studies on lunar samples. IONICS-ESR dating and dosimetry Tokyo 19–39
Trang D, Lucey PG (2019) Improved space weathering maps of the lunar surface through radiative transfer modeling of Kaguya multiband imager data. Icarus 321:307–323
Trang D, Lucey PG, Izenberg NR (2017) Radiative transfer modeling of MESSENGER VIRS spectra: Detection and mapping of sub–microscopic iron and carbon. Icarus 293:206–217
Weber I, Stojic AN, Morlok A, Reitze MP, Markus K, Hiesinger H, Helbert J (2020) Space weathering by simulated micrometeorite bombardment on natural olivine and pyroxene: a coordinated IR and TEM study. Earth Planet Sci Lett 530:115884
Yamada M, Sasaki S, Nagahara H, Fujiwara A, Hasegawa S, Yano H, Otake H (1999) Simulation of space weathering of planet-forming materials: nanosecond pulse laser irradiation and proton implantation on olivine and pyroxene samples. Earth Planets Space 51:1255–1265
Yao JH, Elder KR, Guo H, Grant M (1993) Theory and simulation of Ostwald ripening. Phys Rev B 47(21):14110
Yin T, Li Q, Li X (2019) Experimental investigation on mode I fracture characteristics of granite after cyclic heating and cooling treatments. Eng Fract Mech 222:106740
Zhong J, Xie L, Lee LC, Slavin JA, Raines JM, Dewey RM, Wei Y (2024) North-south plasma asymmetry across mercury's near-tail current sheet. Geophys Res Lett 51(1):e2023GL106266
Zomerdijk-Russell S, Masters A, Korth H, Heyner D (2023) Modeling the time-dependent magnetic fields that bepicolombo will use to probe down into mercury's mantle. Geophys Res Lett 50(2):e2022GL101607